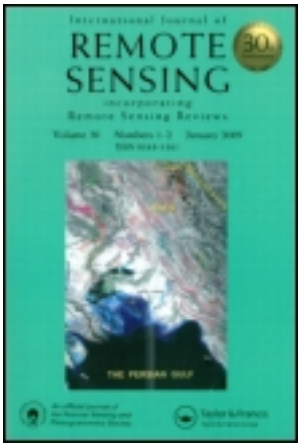

International Journal of Remote Sensing

Publication details, including instructions for authors and subscription information:
http://www.tandfonline.com/loi/tres20

Validation of ERS-2 SAR offshore wind-speed maps in the North Sea

C. B. Hasager Corresponding author [a], E. Dellwik [a], M. Nielsen [a] & B. R. Furevik [b]

[a] Risø National Laboratory, Wind Energy Department, DK-4000 Roskilde, Denmark

[b] Nansen Environmental and Remote Sensing Center, Edvard Griegsvei 3A, N-5059 Bergen, Norway

Available online: 04 Jun 2010

To cite this article: C. B. Hasager Corresponding author, E. Dellwik, M. Nielsen & B. R. Furevik (2004): Validation of ERS-2 SAR offshore wind-speed maps in the North Sea , International Journal of Remote Sensing, 25:19, 3817-3841

To link to this article: http://dx.doi.org/10.1080/01431160410001688286

INT. J. REMOTE SENSING, 10 OCTOBER, 2004,
VOL. 25, NO. 19, 3817–3841

Taylor & Francis
Taylor & Francis Group

Validation of ERS-2 SAR offshore wind-speed maps in the North Sea

C. B. HASAGER*, E. DELLWIK, M. NIELSEN

Risø National Laboratory, Wind Energy Department, DK-4000 Roskilde, Denmark

and B. R. FUREVIK

Nansen Environmental and Remote Sensing Center, Edvard Griegsvei 3A, N-5059 Bergen, Norway

(*Received 4 September 2002; in final form 21 October 2003*)

Abstract. Wind maps are retrieved from ERS-2 Synthetic Aperture Radar (SAR) scenes by the CMOD-IFR2 and CMOD4 algorithms for 61 cases at the Horns Rev site in the North Sea and compared to meteorological *in situ* observations from a mast located 14 km offshore. The *in situ* data are corrected for flow distortion and sea-level changes prior to validating the SAR wind maps. The SAR wind maps are area-averaged by a simple footprint method assuming neutral stability and with three nonlinear weighting footprint methods including correction for stability. From a physical point of view, the latter is more correct. However, between *in situ* and SAR-derived wind-speed estimates comparison results of the nonlinear footprint values are statistically less correlated ($R^2 = 0.73$–0.77) and the standard error (SE) is larger ($> 1.5\,\mathrm{m\,s^{-1}}$) than results from the simple footprint ($R^2 = 0.78$–0.80 and $\mathrm{SE} = 1.3\,\mathrm{m\,s^{-1}}$). The results are found with wind direction determined from wind streaks in the SAR images by Fast Fourier Transform. Using *in situ* wind direction as input to the CMOD-IFR2 and CMOD4 algorithms yields even better linear regression results, e.g. for the simple footprint method $R^2 = 0.88$ and $\mathrm{SE} = 0.9\,\mathrm{m\,s^{-1}}$. SAR wind maps may be useful for mapping of future offshore wind resources.

1. Introduction

Determination of offshore wind speed is an important measure for a number of coastal activities including prediction of wind-power production, construction activities, navigation, fishing, sailing sports, wind surfing, air pollution and other coastal environmental impacts. Wind-speed observations from lighthouses, coastal and offshore masts, ocean buoys and ships have been collected for centuries. More recently, spatial ocean wind-speed observations have become available from satellite remote sensing technologies such as passive microwave, scatterometer, imagettes, altimeter and Synthetic Aperture Radar (SAR). Therefore offshore wind speed and wind direction may now be mapped at various spatial scales and

*Corresponding author; e-mail: charlotte.hasager@risoe.dk

International Journal of Remote Sensing
ISSN 0143-1161 print/ISSN 1366-5901 online © 2004 Taylor & Francis Ltd
http://www.tandf.co.uk/journals
DOI: 10.1080/01431160410001688286

calculated into offshore wind-resource maps, an ultimate goal of the WEMSAR (Wind Energy Mapping using SAR) project based on satellite Earth Observations (EO) data.

Offshore wind resources are currently calculated from long-term meteorological data that are typically obtained from offshore or coastal masts. Such masts are costly to install and operate. Furthermore, wind-speed time series must cover at least 1 year of wind climate to be accurately assessed; hence this method is time consuming and not an ideal situation for offshore wind-farm feasibility studies in the highly competitive market of renewable energy resources. Offshore wind farming is a rapidly growing industry and the prospective output from a wind turbine is a critical component of its economic feasibility. Hence the investment in an offshore wind farm is strongly dependent on optimization analysis of the annual energy production within a region. Therefore wind-speed mapping from satellite imagery may constitute an attractive alternative or additional source of observations (Johannessen and Björgo 2000, Fichaux and Ranchin 2002, Furevik and Espedal 2002) while the limited number of satellite scenes available for a given region as well as the relative accuracy of remote sensing-based wind-speed mapping will reduce the absolute accuracy of wind resource estimation compared to mast observations. The advantages of remote sensing-based wind mapping are that the wind resources may be more quickly assessed from historical archives of satellite scenes, and spatial variability is mapped explicitly.

Ocean wind-speed observations from scatterometer and passive microwave sensors constitute a unique dataset that could be used to produce a global offshore wind atlas. The wind cell spacing is adequate (around $25\,\mathrm{km} \times 25\,\mathrm{km}$ or $50\,\mathrm{km} \times 50\,\mathrm{km}$) and the coverage is almost daily through many years (SSM/I since 1987 (only wind speed), ERS AMI-SCAT since 1991, Quikscat since 1999, MIDORI-2 since 2002 and WindSat since 2003). For regional-scale wind energy mapping, a higher spatial resolution is of interest, especially in the near-coastal zone where most offshore wind farms are currently prospected. SAR images from ERS, Radarsat and Envisat supply high-resolution spatial observations over several years with a less frequent time interval.

This validation study concerns wind speed and wind direction maps retrieved from 61 ERS-2 SAR scenes for a site in the North Sea, Denmark where the largest offshore wind farm in the world started operation in December 2002. The Horns Rev offshore wind farm consists of 80 2 MW wind turbines erected in a grid over an area of $20\,\mathrm{km}^2$ at a distance of 14–20 km offshore. The expected annual output is 600 GW h (http://www.hornsrev.dk/). The wind farm belongs to Elsam, a Danish power company. Since May 1999, meteorological observations from a tall offshore meteorological mast and marine buoy observations have been collected for the wind-farm project and are used within the present validation study. The meteorological *in situ* observations are analysed and compared to SAR wind-speed maps that are area-averaged using footprint theory.

From a physical point of view the footprint area-averaging method is the most correct comparison method when comparing the spatial snapshots of wind speed from SAR to the *in situ* wind-speed time series. Each SAR resolution cell within the upwind area of the mast is weighted by the fraction of its importance to the total wind speed observed. The size of the elliptical footprint is a function of measurement height and atmospheric stability.

The main objective of the work is to validate a simple, widely used, and robust method for wind retrieval from SAR—the C-band transfer model—with accurate

mast observations for a large dataset. Furthermore, we will investigate if the correlation is dependent on the method used for averaging the SAR data.

The SAR wind-speed maps are retrieved from the CMOD4 (Stoffelen and Anderson 1997) and CMOD-IFR2 (Quilfen *et al.* 1998) algorithms valid for open seas. The empirical algorithms are based on the physical link between the normalized radar cross-section and the ocean surface roughness generated by the surface wind speed. The wind stress is translated into a spectrum of capillary and short gravity waves as a function of surface wind speed, wind direction and look angle. The wind speed retrieved in the coastal zone may be modified compared to that of the open seas due to variations in the surface roughness. Error estimation on SAR wind-speed maps is essential for applied wind resource estimation as the wind-power potential is proportional to the cube of the mean wind speed. The possible sources of error on SAR-derived wind maps are discussed.

2. Satellite SAR and wind maps

Satellite SAR scenes in C-band are available from ERS-1 July 1991 to June 1995, ERS-2 since April 1995 to present, Radarsat-1 since November 1995 to present (Kramer 1996), and Envisat ASAR since March 2002 to present (http://envisat.esa.int/). Radarsat-2 is planned for launch in 2004 with a lifetime of 7 years. In the current study only ERS-2 SAR scenes from the European Space Agency (ESA) are investigated. ERS-2 has a repeat track of about 10 days at mid-latitudes with local recording times around 10.30 in the descending mode and 21.30 in the ascending mode (http://earth.esa.int/) (Attema *et al.* 2000).

The ERS SAR emits C-band microwave radiation in angles between 20° and 26° to the right side of the flight direction. The spatial resolution in ERS SAR is 26 m in range (antenna look direction) and between 6 and 30 m in azimuth (in-flight direction) (Attema *et al.* 2000, Horstmann *et al.* 2000). An ERS SAR scene is 100 km × 100 km. The measured backscatter is transformed into normalized radar cross-section, Φ_0 (dB), by calibrating the data. Derived from open ocean collocations, Φ_0 is dependent on the relative wind direction (N in °, $N=0°$ for a wind blowing against the radar), the local radar beam incidence angle (α in °) of the illuminated area, and mean wind speed at 10 m above the sea surface (u in $\mathrm{m\,s^{-1}}$) expressed as

$$\sigma_0 = B_0(1 + B_1\cos(\phi) + B_2\cos(2\phi)) \tag{1}$$

B_0, B_1, B_2 are coefficients that depend on α and u (Offiler 1994, Quilfen *et al.* 1998). The accuracy of the model in equation (1) is ±20° solving for wind direction and $\pm 2\,\mathrm{m\,s^{-1}}$ or 10% in rms. when solving for wind speeds between 2 and $24\,\mathrm{m\,s^{-1}}$ (Stoffelen and Anderson 1993). According to Offiler (1994) and Vachon and Dobson (1996) the accuracy on wind speed is better: $\pm 1.5\,\mathrm{m\,s^{-1}}$ and $\pm 1.2\,\mathrm{m\,s^{-1}}$, respectively.

The SAR wind-speed retrieval method originates from C-band scatterometer models such as CMOD4 (Stoffelen and Anderson 1997) and CMOD-IFR2 (Quilfen *et al.* 1998). These are based on correlation analysis between global ocean buoy data and/or European Center of Medium Range Forecast (ECMWF) ocean wind field results and C-band scatterometer data. Scatterometer data allow both wind speed and wind direction (with 180° ambiguity) to be retrieved simultaneously, whereas with SAR either wind speed or wind direction is needed as input in equation (1). However for most SAR scenes, the wind direction (with 180° ambiguity) can be determined from the direction of the so-called wind streaks.

These are linear features aligned with the wind direction resulting from atmospheric roll vortices or Langmuir cells in the sea. The dominant direction of the streaks can be derived from the long-wave part of the image spectra. In the current study image spectra are produced using the two-dimensional Fast Fourier Transformation (2-D FFT) (Gerling 1986, Lehner *et al.* 1998, Furevik *et al.* 2002).

The short-wave part of the spectrum is periodic disturbances of the ocean surface on scales of 1–30 cm, i.e. capillary waves and short gravity waves (Thompson and Beal 2000). Capillary waves with periods of less than 0.1 s and short gravity waves respond quickly to changes in wind speed (Knauss 1978, Garratt 1992). The timescale of the generation of Bragg resonance waves is around $0.2\,s^{-1}$ for a wind speed of $3\,m\,s^{-1}$ and $0.5\,s^{-1}$ for $5\,m\,s^{-1}$ (Askari 2001) i.e. near instantaneous. SAR effectively map the near surface wind in snapshots. In validation studies the SAR wind-mapping timescale has to be considered in regard to time-average values of *in situ* wind observations.

Errors in SAR wind-speed retrieval is dependent on the input to the wind-retrieval algorithm, i.e. α, σ_0 and N and the wind retrieval algorithm itself, i.e. the accuracy of the empirical coefficients. The error associated with α is negligible for ERS SAR because of the narrow band of incidence angles. The errors associated with σ_0 include three independent sources of error: (1) SAR calibration accuracy, (2) effect of speckle noise, and (3) oceanographic and atmospheric noise.

The error in SAR wind speed associated with uncertainty in relative wind direction (N) is assessed from experimental research. For an incidence angle of 23° (in the middle of the ERS SAR incidence angle interval), the results show an error $<10\%$ for all wind speeds within 15° of upwind, downwind and crosswind angles. However for winds at angles of $\pm 45°$ from crosswind, the error is about 20% for wind speeds $>7\,m\,s^{-1}$ (Korsbakken *et al.* 1998, Horstmann *et al.* 2000).

Errors associated with the CMOD wind retrieval coefficients relate to the empirical methodology of determining these from collocated pairs of buoys and atmospheric model results. The correlation analysis between the coarse grid cells of the scatterometer and, for example, buoy data can suffer from smaller scale gradients within the cells that are averaged out. Furthermore calibration data from buoys and ships may suffer errors due to flow distortion, tilting and displacement (Brown 2000a,b, Atlas *et al.* 2001). Improvements to the current algorithms are ongoing as the global dataset collocated with buoys and model data becomes larger. CMOD5 (Figa-Saldaña *et al.* 2002) has been recently developed to better account for especially high wind speeds.

The ideal condition for a validation study is an accurate collocation between the SAR wind-speed maps and *in situ* observations. Meteorological masts have the advantage of well-known positions and solid mounting (versus buoys and ships), hence only the geometrical rectification of satellite images introduces error. This is a minor problem in coastal regions where sub-pixel accuracy may typically be obtained through ground control points from maps (Lillesand and Kiefer 1987). Mast observations typically have a high quality, but it is important to correct for land surface orography if placed at or near the coast (Hasager *et al.* 2002). Atmospheric stability effects may also be important. Marine internal boundary layers develop for offshore flow. In stable stratification the SAR wind speed may be significantly smaller than the wind-speed observations at higher levels, i.e. a larger gradient than predicted by the logarithmic wind profile occurs in a stable marine internal boundary layer (Stull 1991).

Generally, averaging SAR wind speed within a box collocated with *in situ*

observations is used for comparing the mean wind speed. Box sizes of 4–64 km^2 have been used (Sikora *et al.* 2002, Katsaros *et al.* cited in Mourad 1999, Monaldo *et al.* 2001, Vachon and Dobson 1996). From a physical point of view, the optimal comparison method between SAR wind-speed maps and *in situ* observations is performed through the footprint methodology. This ensures a correct selection of grid cells in the wind map in response to the observed wind at a certain height above sea level.

3. Footprint methodology

The theory on scalar footprints originates from Gash (1986) and is sketched in figure 1. The air is advected to a sensor at a given height from the upwind source area. In the area close to the sensor there is a large influence whereas the area further away has lesser influence. The footprint area-averaging method has mainly been used for land surfaces, but an example by Smedman *et al.* (1999) shows the use of footprint theory in a marine study.

Gash (1986) proposed a crosswind-integrated footprint of the type

$$f^{y}(x) = \frac{A}{x^2}\exp\left\{-\frac{A}{x}\right\}, \quad \text{for } x > 0. \tag{2}$$

The length scale $A = uz/6u_*$ depends on a uniform advection velocity (u in $m\,s^{-1}$), the flux measurement height (z in m), and friction velocity (u_* in $m\,s^{-1}$). The footprint is derived on the assumption that the vertical profile of a plume from a ground source has an exponential shape and that the advection speed is considered uniform. The x-axis is in the upwind direction and the integral from the mast position to infinity is unity. The maximum is found at the distance $x = A/2$ and the downwind footprint integral is

$$F^{y}(x) = \exp\left\{-\frac{A}{x}\right\}, \quad \text{for } x > 0 \tag{3}$$

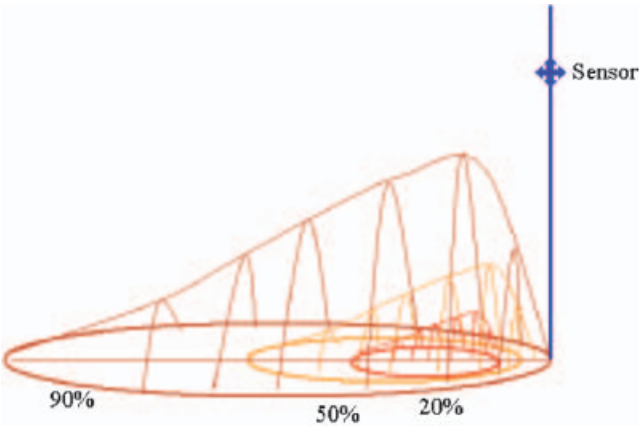

Figure 1. Sketch of the weighted footprints relating to a sensor at a given height. The area giving a certain percentage of influence to the signal is shown at 20%, 50% and 90% intervals.

For neutral conditions the formula

$$X_P = \frac{z}{\kappa^2} \ln\left(\frac{z}{z_0}\right) \Big/ \ln\left(\frac{100\%}{P}\right) \tag{4}$$

expresses that a per cent fraction, P (%), of the measured flux derives from within an upwind distance X_P (m), z_0 (in m) is the roughness and κ is the von Karmán constant. Because of turbulence in the lateral direction, the footprint area is elliptical.

Two newer footprint methods based on Horst and Weil (1994) and Hsieh *et al.* (2000) consider stability effects. Details are given in the Appendix. Simply described the footprint is shorter for unstable conditions and longer for stable conditions for a given height. Meteorological data on stability are available in the current study and footprint results are included to clarify if using these advanced methods may improve validation results.

4. The investigated datasets

A series of 61 ERS-2 SAR scenes in the Precision (PRI) format from the Horns Rev area in the North Sea, Denmark are retrieved from ESA. The scenes are calibrated by the SAR Tool Box software (http://earth.esa.int/stbx/documentation/manual/stbx_V-5_5.html). The determination of wind direction in the SAR scenes is performed with 2-D FFT derived image spectra (Gerlich 1986). The dominant SAR streak direction is determined in blocks of 12.5 km × 12.5 km grid cells by the 2-D FFT routine both over land and sea. The 180° ambiguity is then removed using the *in situ* wind direction. The total of 64 arrows covering each scene is visually inspected. Those over land and those mapping other features than wind direction over the sea are manually deselected. An example is shown in figure 2. The remaining arrows are used to interpolate wind directions for the whole scene.

For each scene the map of wind streak is then used as input to the CMOD4 and CMOD-IFR2 algorithms. An alternative wind map is calculated per scene using the *in situ* wind direction as input to the two models. A total of 248 wind speed maps are calculated. Each wind-speed map covers an area of 100 km × 100 km and the pixel size is 400 m × 400 m, i.e. reduced from the original resolution.

The averaging of cells (multi-looking) is performed to reduce speckle noise. The speckle noise is due to scattering of coherent electromagnetic waves by rough surfaces (Goldfinger 1982). To reduce the error from speckle noise, a sufficiently large equivalent number of looks (ENL) are required. The backscatter (intensity) in homogeneous areas follows a gamma distribution (Oliver and Quegan 1998) and the definition of ENL can be expressed as the ratio between mean of Φ_0 and the variance of Φ_0

$$\mathrm{ENL} = \frac{\text{Mean } \sigma_0}{\text{Var } \sigma_0} \tag{5}$$

and the determination of variation of speckle expressed as $\pm$ the standard deviation (SD) in dB

$$\text{Mean } \sigma_0 \pm \mathrm{SD} = \text{mean } \sigma_0 \left(1 \pm \frac{1}{\sqrt{\mathrm{ENL}}}\right) \tag{6}$$

For one scene (from 2 September 2001) containing a homogeneous area, ENL is calculated from equation (5) within a box area outlined in figure 3. The result on

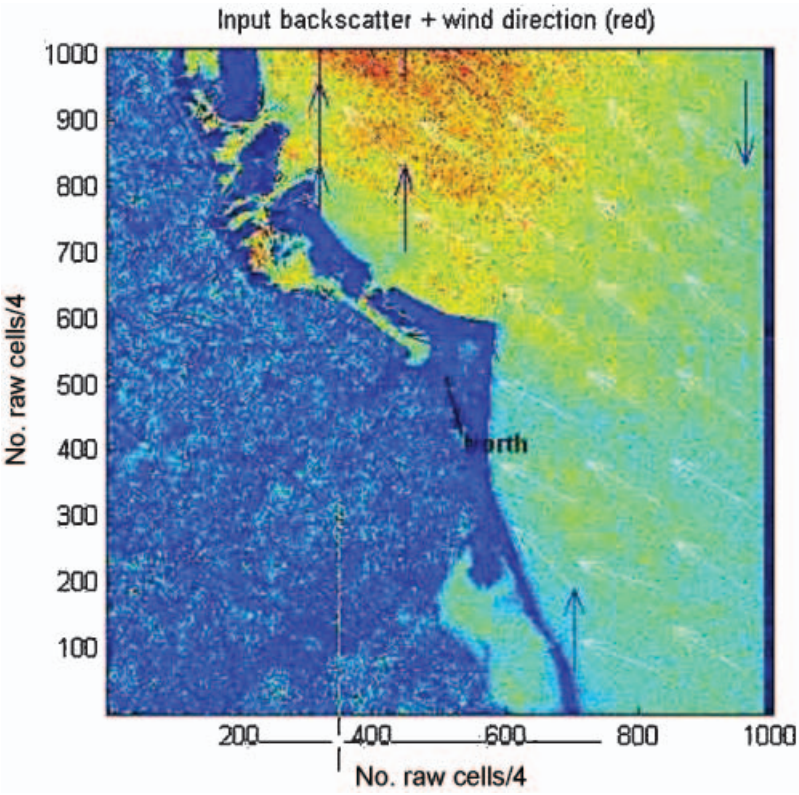

Figure 2. Selection of SAR streak direction arrows in the case of 23 October 2003 showing the intensity in image spectra and the selected arrows (in white) and those not selected (in black) due to mis-orientation. The *in situ* wind direction is 128°, hence there is a 180° ambiguity correction in this case. (Intermediate image is not georeferenced.)

ENL as a function of grid size is also shown in figure 3. For the highest resolution ENL is around 3 as expected and increasing with lower resolution. However for the lowest resolutions tested (degradation to cells of 1600 m × 1600 m and 200 m × 2000 m), the statistics become unreliable due to too few samples within the selected box. ENL is >350 for these resolutions. Variation due to speckle noise is calculated by equation (6), and the results are listed in table 1. For the 400 m resolution ENL is ~170 hence speckle noise introduces error around 0.3 dB. This is within the radiometric accuracy of ERS-1 and −2 SARs of ±0.4 dB (Attema *et al.* 2000). For lower resolution, e.g. at 2000 m, the speckle noise is below 0.2 dB. For very high wind speeds with backscatter of around 0 dB, the accuracy may be lower, depending on the calibration procedure (Horstmann *et al.* 2000). The effect of azimuth smearing and velocity bouncing due to longer waves may be seen in the SAR images with a grid cell size of 400 m × 400 m. However, the cells are further averaged prior to validating SAR winds, thereby minimizing this effect.

At Horns Rev a long-term data series of wind speed, wind direction and air temperatures are continuously sampled into 10-min mean values from sensors mounted at a tall mast located 14 km offshore from the coast of Jutland (Neckelmann and Petersen 2000, Sommer 2003). The analysed time series cover the

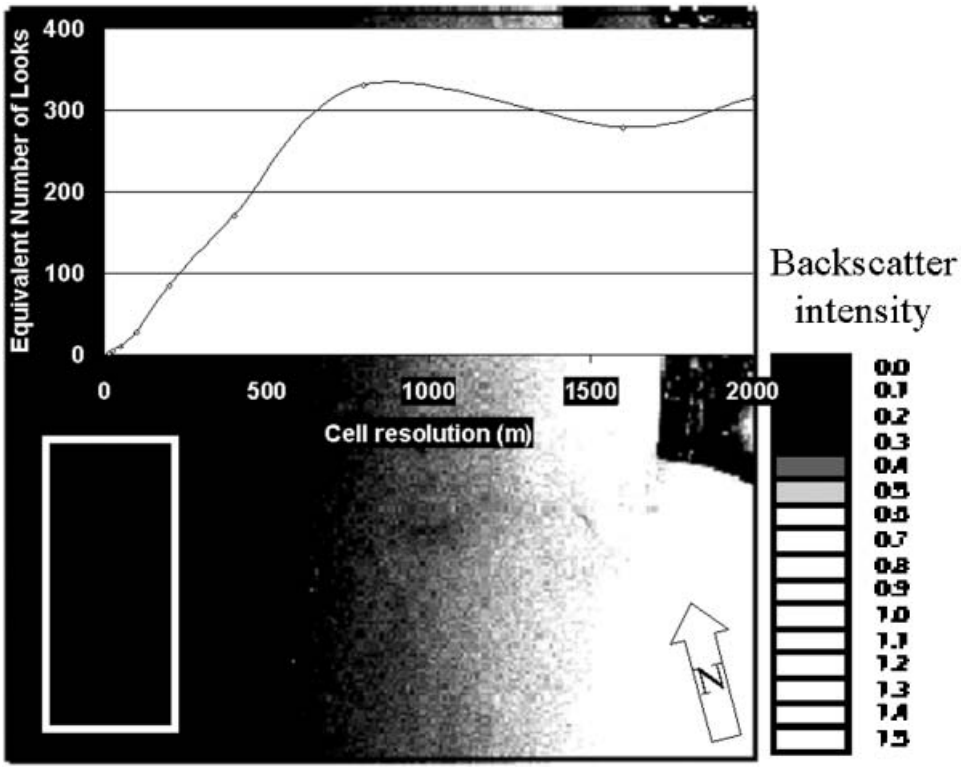

Figure 3. ERS-2 SAR backscatter intensity map from Horns Rev in the North Sea on 2 September 2001 at 10:26 UTC showing a rectangular box in a homogeneous area in which an empirical study on equivalent number of looks (ENL) is performed in relation to spatial grid scales. ENL is graphed as a function of averaged cell size in the upper part of the figure. (Intermediate image is not georeferenced.)

period from 16 May 1999 to 23 October 2001, i.e. a time prior to the installation of the Horns Rev offshore wind farm. The Horns Rev offshore area and the position of the meteorological mast are shown in figure 4.

The wind speed is measured at four levels. For the three lower levels identical cup anemometers are placed on booms in two directions. One boom is pointing to the south-west at 225° and the other boom to the north-east at 45°. So for the sector 135–315°, the south-west data are analysed, and for the 315–135° sector, the north-east data are analysed. The reason for two booms in opposite directions is to avoid flow distortion from the tower itself in the dataset. The wind speeds are measured at 15, 30, 45 and 62 m above DNN (Danish mean sea level), the air

Table 1. Variation of speckle noise expressed as ± the standard deviation (SD) in dB for equivalent number of looks (ENL).

	ENL						
	3	10	50	100	200	300	400
Mean Φ_0+SD	2.0	1.2	0.6	0.4	0.3	0.3	0.2
Mean Φ_0−SD	3.7	1.7	0.7	0.5	0.3	0.2	0.2

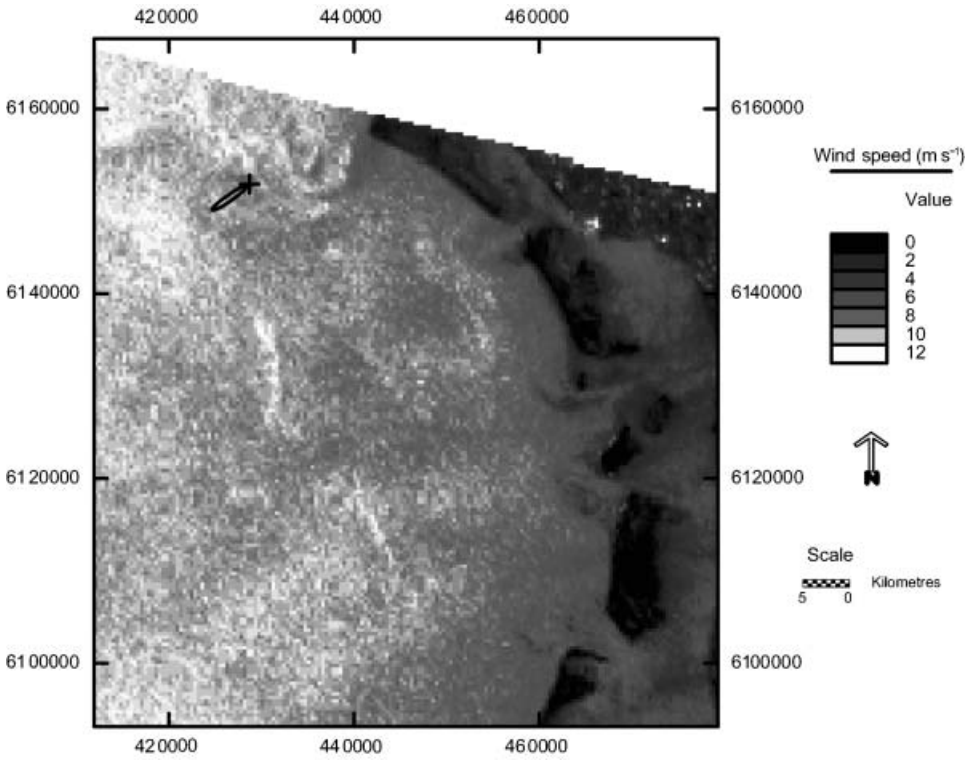

Figure 4. Ocean wind-speed map from ERS-2 SAR derived by CMOD-IFR2 at the Horns Rev site in the North Sea, Denmark. A meteorological mast is positioned at 55°30′27.82″ N, 7°52′30.05″ E indicated with + and the simple ellipse-shaped footprint upwind of the mast is shown. The wind is 10.5 m s^{-1} from the south-west at 10 m. The scene shown is from 1 February 2000 at 10.28 UTC with UTM (zone 32) coordinates, WGS84.

temperatures at 13 and 55 m, and the wind direction at 60 m. The data are stored as 10-min mean values and the accuracy on wind speed is 1%. The *in situ* wind direction data are of a very high quality and may therefore serve as a test-bed for how accurate SAR wind-speed maps may become providing wind streaks perfectly delineate the true wind directions. The selected scenes and the meteorological observations at the time of the satellite overpasses are listed in table 2 and the wind speed calculated by CMOD-IFR2 algorithm for one case (1 February 2000) is shown in figure 4.

5. Analysis of the atmospheric observations

The analysis has two objectives. The first objective is to estimate the 10 m wind speeds for comparison to the SAR wind-speed maps. The second is to estimate the atmospheric stability in order to facilitate footprint calculations including stability effects.

The original atmospheric observations of continuous 10-min mean wind-speed values are averaged into 60-min mean values centred at the time of satellite overpass. The wind speed at 10 m is found from a log–linear extrapolation of winds at four higher levels at 15, 30, 45 and 62 m assuming the logarithmic wind profile

Table 2. ERS-2 SAR scenes listed with time, orbit, track and frame numbers. The column 'arrows' indicates the number of selected SAR wind streak blocks. The meteorological observations at the Horns Rev site at the time of the satellite overpasses are the mean wind speed, u at 10 m, mean wind direction at 60 m and the bulk Richardson's number Ri averaged to 1-h mean values centred at the ERS SAR acquisition times. The DNN deviation (δ) is the sea-level variation from Danish Normal Zero (DNN) at the closest 20 min. The atmospheric measurements are collected by Elsam Engineering. δ is calculated at the Horns Rev site from sea-level data in Esbjerg Harbour collected by the Danish Meteorological Institute and sea-level data is from Elsam Engineering.

	Date	Time (UTC)	Orbit	Track	Frame	Arrows (−)	*In situ* u (10 m) ($m\,s^{-1}$)	*In situ* wind direction (°)	Ri (m)	DNN δ (m)
1	20 May 99	21:30	21340	444	1107	8	7.8	124	45.4	−0.26
2	20 Jun. 99	10:31	21777	380	2482	18	10.2	223	−0.1	0.03
3	21 Jun. 99	21:24	21798	401	1107	6	10.1	315	−1.3	0.42
4	6 Jul. 99	10:28	22006	108	2486	12	3.7	298	−13.3	−0.22
5	10 Jul. 99	21:27	22070	172	1107	6	4.2	73	0.2	0.35
6	29 Jul. 99	21:30	22342	444	1107	28	5.6	34	−0.1	−0.47
7	10 Aug. 99	10:28	22507	108	2493	28	11.2	329	−2.5	0.61
8	30 Aug. 99	21:24	22800	401	1107	7	7.0	293	−2.0	−0.41
9	18 Sept. 99	21:27	23072	172	1107	13	5.1	96	−4.3	0.08
10	3 Oct. 99	10:31	23280	380	2493*	46	11.9	240	−0.3	0.44
11	7 Oct. 99	21:30	23344	444	1107	50	10.4	275	−0.4	0.51
12	19 Oct. 99	10:28	23509	108	2493	20	8.9	88	−1.1	−0.28
13	23 Nov. 99	10:28	24010	108	2493	4	1.6	232	−0.8	0.52
14	16 Dec. 99	21:30	24346	444	1107	40	9.9	245	−144.6	0.34
15	16 Jan. 00	10:31	24783	380	2493*	23	7.7	305	0.0	0.09
16	1 Feb. 00	10:28	25012	108	2493	20	10.5	235	0.0	0.71
17	24 Feb. 00	21:30	25348	444	1107	43	6.0	249	0.0	−0.03
18	7 Mar. 00	10:28	25513	108	2493	19	12.1	255	0.0	0.33
19	26 Mar. 00	10:31	25785	380	2475*	15	4.4	126	−3.0	−0.47
20	11 Apr. 00	10:28	26014	108	2486	15	6.7	130	−5.6	−0.4
21	15 Apr. 00	21:27	26078	172	1107	24	5.2	96	−0.1	0.35
22	4 May 00	21:30	26350	444	1107	10	4.6	110	2.0	−0.23
23	16 May 00	10:28	26515	108	2493	37	4.7	182	−0.1	0.27
24	4 Jun. 00	10:30	26787	380	2482	14	7.9	90	−1.1	0
25	5 Jun. 00	21:24	26808	401	1107	3	6.9	100	−0.2	0
26	20 Jun. 00	10:28	27016	108	2486	7	3.9	215	0.2	−0.46
27	24 Jun. 00	21:27	27080	172	1107	12	6.2	315	−3.4	0.29
28	9 Jul. 00	10:31	27288	380	2482	11	6.6	174	−4.2	−0.01
29	13 Jul. 00	21:30	27352	444	1107	41	6.1	258	−1.4	0.35
30	25 Jul. 00	10:28	27517	108	2482	4	3.5	110	−0.2	−0.16
31	13 Aug. 00	10:31	27789	380	2482	17	4.0	128	−0.5	0.35
32	14 Aug. 00	21:24	27810	401	1107	6	5.9	193	0.1	−0.18
33	29 Aug. 00	10:28	28018	108	2482	8	2.7	235	−9.7	0.27
34	2 Sept. 00	21:27	28082	172	1107	9	12.0	17	−0.3	−0.59
35	17 Sept. 00	10:31	28290	380	2482	33	8.0	110	−1.2	−0.4
36	21 Sept. 00	21:30	28354	444	1107	57	12.1	120	−0.4	0
37	23 Oct. 00	21:24	28812	401	1107	4	9.3	202	0.0	0.62
38	7 Nov. 00	10:28	29020	108	2482	8	8.2	144	−8.6	0.52
39	11 Nov. 00	21:27	29084	172	1107	34	13.3	200	−0.1	0.3
40	26 Nov. 00	10:31	29292	380	2482	43	12.6	149	−1.0	0.17
41	30 Nov. 00	21:30	29356	444	1107	36	6.8	187	−0.2	−0.25
42	12 Dec. 00	10:28	29521	108	2482	18	8.5	203	0.0	0.43
43	15 Dec. 00	10:33	29564	151	2482*	60	15.4	320	−0.1	0.09
44	1 Jan. 01	21:24	29814	401	1107	5	8.3	197	0.0	0.01

Table 2. (*Continued*).

	Date	Time (UTC)	Orbit	Track	Frame	Arrows (−)	*In situ* u (10 m) ($m\,s^{-1}$)	*In situ* wind direction (°)	*Ri* (m)	DNN δ (m)
45	8 Feb. 01	21:30	30358	444	1107	20	4.3	348	0.0	0.05
46	20 Feb. 01	10:28	30523	108	2482	5	6.8	306	0.1	0.37
47	12 Mar. 01	21:24	30816	401	1107	5	7.8	202	0.0	−0.33
48	27 Mar. 01	10:28	31024	108	2482	25	11.3	127	−0.5	−0.46
49	15 Apr. 01	10:30	31296	380	2482	9	3.9	304	−0.2	−0.09
50	19 Apr. 01	21:30	31360	444	1107	23	6.0	49	−1.5	0.55
51	1 May 01	10:28	31525	108	2482	24	8.4	341	−0.9	−0.14
52	5 Jun. 01	10:27	32026	108	2482	6	5.2	233	−4.3	0.2
53	29 Jul. 01	10:30	32799	380	2482	18	5.7	223	−1.1	0.15
54	30 Jul. 01	21:23	32820	401	1107	5	8.8	278	−0.8	0.63
55	14 Aug. 01	10:27	33028	108	2482	6	7.6	233	−0.3	0.28
56	18 Aug. 01	21:26	33092	172	1107	30	8.1	94	−0.4	−0.09
57	2 Sept. 01	10:29	33300	380	2482	32	10.2	246	−0.3	0.5
58	6 Sept. 01	21:29	33364	444	1107	27	8.8	270	−0.4	−0.36
59	18 Sept. 01	10:26	33529	108	2482	15	7.8	55	−1.3	0.23
60	8 Oct. 01	21:23	33822	401	1107	11	11.4	184	−0.1	0.01
61	23 Oct. 01	10:26	34030	108	2482*	26	12.8	128	−0.4	−0.55

*The frame does not cover the site but is from the near vicinity.

for neutral conditions (Stull 1991)

$$u(z) = \frac{u_*}{\kappa}\left(\ln\frac{z-\delta}{z_0}\right) \tag{7}$$

where z (in m) is the height, κ (–) is the von Karmán constant, z_0 (m) is the roughness length and u_* ($m\,s^{-1}$) is the friction velocity to be valid. δ (m) is sea-level deviation from DNN.

In order to correct the wind-profile data for sea-level changes, the sea-level observations from a buoy at Horns Rev are compared and correlated to the Esbjerg Harbour sea-level data for the first 10 days of July 1999. Only during this time the water level instrument functioned well at Horns Rev. The correlation function is estimated as $\delta_{\mathrm{HornsRev}} \approx 0.68\delta_{\mathrm{EsbjergHarbour}}$ where δ (in m) is the sea-level deviation from the DNN at the two sites. Part of the two time series is shown in figure 5, and the mean sea level at the Horns Rev site at the time of the satellite overpasses is summarized in table 2. The water level deviated within +0.7 m to −0.6 m from the DNN. The sea-level deviation from DNN is added to the height z in equation (7) prior to calculating the 10 m wind speed from the wind observations.

For estimating the atmospheric stability the bulk Richardson number Ri_{B} is calculated according to

$$Ri_{\mathrm{B}} = \frac{g}{T}\frac{[\theta(z_1)-\theta(z_2)]/(z_1-z_2)}{([u(z_3)-u(z_4)]/(z_3-z_4))^2} \tag{8}$$

with $g = 9.81\,m\,s^{-2}$, and T and θ signifying absolute and potential temperature, respectively. The heights are $z_1 = 55$ m, $z_2 = 13$ m, $z_3 = 62$ m and $z_4 = 15$ m in our case. The results on wind speed at 10 m, wind direction and Ri_{B} are listed in table 2. Originally, stability corrections to the logarithmic functions were included. In general, the assumption of neutral profiles, although incorrect, yielded better results, which is why no results for atmospheric stability corrected wind speed are

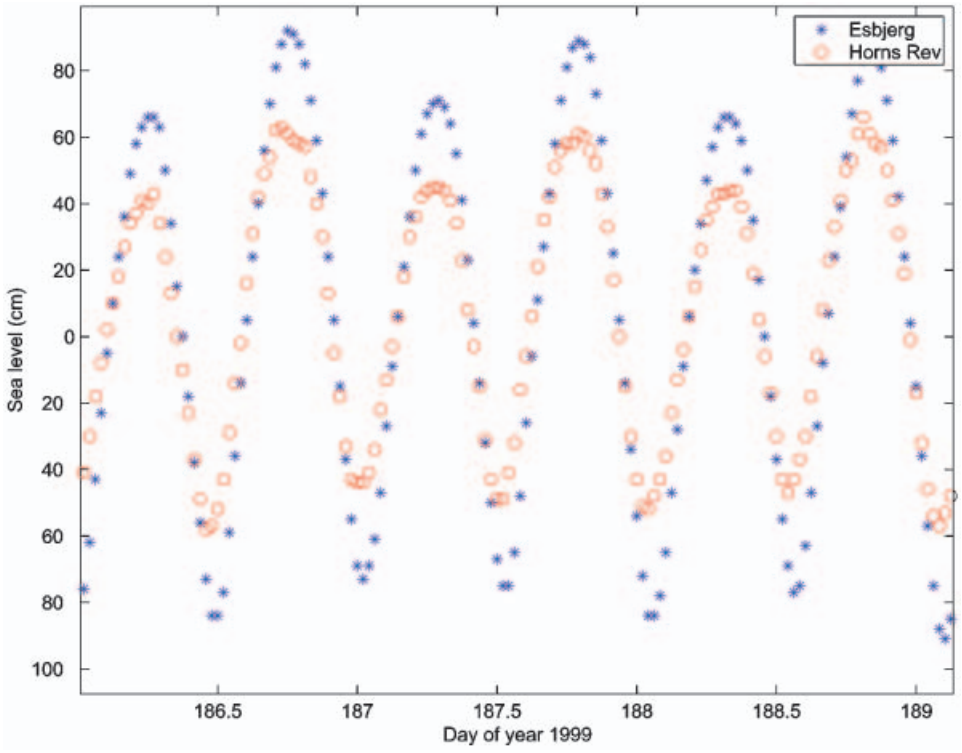

Figure 5. Horns Rev mean sea level compared with the sea level in Port of Esbjerg.

shown. The reason for rather poor results when including stability correction may be that the Ψ functions (see, e.g., Stull 1991) over the sea are poorly known. Furthermore wind profiles on an hourly timescale may have a high degree of scatter compared to an ideal profile (R. J. Barthelmie 2002, personal communication).

6. Comparison of SAR wind maps and *in situ* mast data

Wind-speed maps from 61 SAR scenes are retrieved both with the CMOD4 (Stoffelen and Anderson 1997) and CMOD-IFR2 (Quilfen *et al*. 1998) based on the assumption that the wind direction (equation (1)) is known either (1) from streak direction analysis in the SAR scenes or (2) *a priori* from the meteorological *in situ* data.

The first two resulting wind map datasets, SAR_{streak_CMOD4} and $SAR_{streak\_CMOD\text{-}IFR2}$, are calculated from CMOD4 and CMOD-IFR2, respectively, based on wind streaks. The second two resulting datasets, $SAR_{in\ situ\_CMOD4}$ and $SAR_{in\ situ\_CMOD\text{-}IFR2}$, are based on *in situ* wind direction data from the wind vane on the offshore meteorological tower.

The four sets of wind-speed maps are used in four types of footprint area-averaging methods (Gash 1986, Horst and Weil 1994, Hsieh *et al*. 2000, Hasager *et al*. 2001) (refer to the Appendix). SAR-based wind speeds from each of the footprint results are compared to the *in situ* wind speed (§6.1) and proxy results are compared to *in situ* wind speed for cases with missing SAR data in the footprint (§6.2). Furthermore, the SAR wind streak direction and *in situ* wind direction are compared (§6.3).

6.1. *Footprint comparisons*

Simple footprints (Hasager *et al.* 2001) are calculated for neutral conditions based on equation (4). For the 10 m level and assuming $z_0 = 0.0002$ m, the footprint ellipse for a 90% contribution has a semi-major axis of 2732 m and a semi-minor axis of 482 m, i.e. a total area of 4.1 km^2 covering around 25 resolution cells as the SAR wind-speed maps are gridded at 400 m × 400 m. The area average is not weighted in regard to local position within the footprint but is a uniform average, a similar approach as to that of a land surface flux study based on satellite sensor data (Bastiaanssen *et al.* 1998). The speckle noise within the footprint is reduced to <0.3 dB and this translates to an error on wind speed of <0.5 m s^{-1}. The error due to speckle noise within the simple footprint is below the instrument noise level.

In 56 out of 61 cases it is possible to area-average over the elliptical upwind area. In the last five cases the ellipses stretched into areas of no SAR data. Therefore a box area of a size comparable to the simple footprint was drawn in the vicinity of the mast and used as a proxy. Results from the simple footprint method plotted against *in situ* wind speeds are shown in figure 6(*a*) for the $\mathrm{SAR}_{\mathrm{streak\_CMOD4}}$ and $\mathrm{SAR}_{in\ situ\_\mathrm{CMOD4}}$ wind data, and for the Gash (1986) footprints in figure 6(*b*). The linear regression results are listed in table 3.

From figure 6 and table 3 it is clear that *in situ* 10 m wind speeds typically are higher than those retrieved from the SAR wind maps. For the CMOD4 the bias is -0.3 m s^{-1}, whereas the bias for the CMOD-IFR2 is -0.6 m s^{-1}. From table 3 it is seen that the bias is negative also for the footprints including stability correction (Horst and Weil 1994, Hsieh *et al.* 2000). The smallest bias (-0.1 m s^{-1}) is found using the Gash (1986) footprint method on CMOD4 wind data. However, the correlation coefficient from the simple footprint method (Hasager *et al.* 2001) is higher than for all three other footprint methods which use weighting functions for each pixel as a function of position. Furthermore the standard deviation by the simple footprint is the smallest of all (down to 1.3 m s^{-1}). The above results are based on wind directions retrieved from SAR streaks in the satellite scenes.

The *in situ* wind directions from the wind vane are used as input to the CMOD4 and CMOD-IFR2 algorithms resulting in the wind-speed maps, $\mathrm{SAR}_{in\ situ\_\mathrm{CMOD4}}$ and $\mathrm{SAR}_{in\ situ\_\mathrm{CMOD\text{-}IFR2}}$. Based on these maps, SAR wind speeds are calculated using four footprint methods and the linear regression results between *in situ* wind speed and SAR wind speed are listed in table 3. It is interesting to notice that the correlation increased and the standard error decreased for all four footprint area-averaging methods when using *in situ* wind directions as opposed to SAR streak directions. The simple footprint (Hasager *et al.* 2001) again performed better compared to the nonlinear footprint methods, and as above the CMOD4 is in better agreement with *in situ* wind-speed observations than CMOD-IFR2. However, the bias increased for all cases when using the wind vane data instead of SAR streak direction. The best overall correlation result is found for the simple footprints calculated from the CMOD4 wind-speed maps using *in situ* wind directions. The R^2 increased from 0.78 to 0.88 and the standard error reduced from 1.33 to 0.90 m s^{-1} but at the same time the bias increased from -0.3 to -0.5 m s^{-1}.

6.2. *Footprint and proxy comparison*

In five out of 61 cases the retrieved SAR wind-speed map did not contain the area in which the footprint ellipse is placed. In these cases a box area is used as a proxy. The proxies are of sizes similar to the simple footprint and the proxies are

located in close vicinity to the mast. The linear regression results when including proxy data is listed in table 3 for the simple footprint method. The bias increases dramatically, e.g. from $-0.3\,\mathrm{m\,s^{-1}}$ to $-1.2\,\mathrm{m\,s^{-1}}$ based on CMOD4 with input of SAR wind streak directions. The five cases with proxy data are marked in table 2.

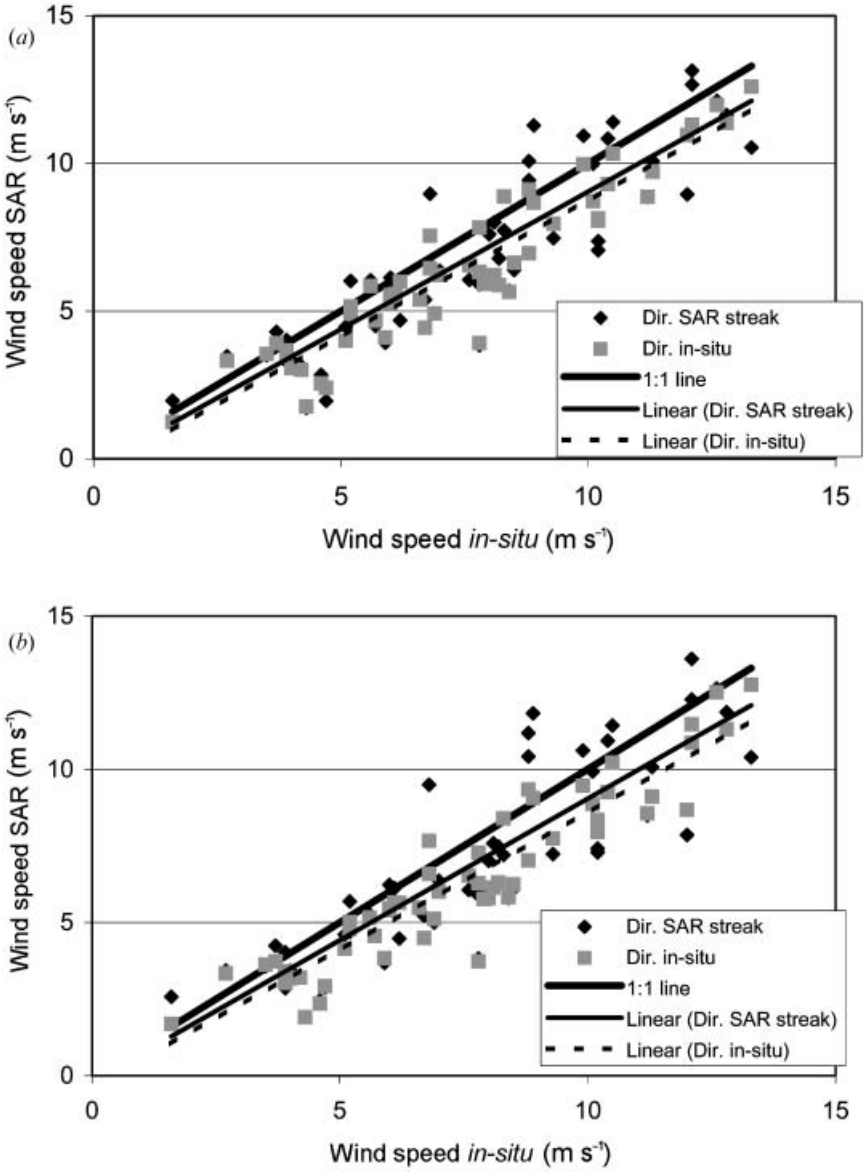

Figure 6. Wind speed at 10 m measured from the *in situ* meteorological mast on the abscissa and calculated from SAR wind-speed maps based on *in situ* wind direction (Dir. *in situ*) and SAR wind streak direction (Dir. SAR streak) on the ordinate axes with linear regression lines and a 1:1 line include for (*a*) the Hasager *et al.* (2001) footprint, (*b*) the Gash (1986) footprint. The regression results are listed in table 3.

Table 3. Linear regression equation results, correlation coefficients (R^2) and standard error (SE) in $m\,s^{-1}$ for four types of footprint models and four types of wind-speed maps calculated by the CMOD4 and CMOD-IFR2 algorithms using wind direction input for SAR streak directions retrieved from satellite scenes and using wind direction from *in situ* wind vane meteorological observations. The number of cases (n) is listed. The proxies are small boxes taken instead of elliptic footprints. These are taken in five cases where no data were available within the footprints.

		Wind direction input from *in situ* meteorological observation			Wind direction input from SAR streak			
	C-model	Regression equation	R^2	SE ($m\,s^{-1}$)	Regression equation	R^2	SE ($m\,s^{-1}$)	Cases n
Footprints only								
Gash (1986)	CMOD4	$y=0.902x–0.398$	0.870	0.92	$y=0.924x–0.120$	0.745	1.49	56
	CMOD-IFR2	$y=1.078x–0.939$	0.857	1.14	$y=1.079x–0.581$	0.772	1.58	56
Hasager *et al.* (2001)	CMOD4	$y=0.930x–0.516$	0.881	0.90	$y=0.932x–0.276$	0.784	1.33	56
	CMOD-IFR2	$y=1.102x–1.025$	0.865	1.14	$y=1.087x–0.635$	0.800	1.46	56
Horst and Weil (1994)	CMOD4	$y=0.901x–0.406$	0.866	0.94	$y=0.924x–0.200$	0.736	1.52	56
	CMOD-IFR2	$y=1.077x–0.951$	0.854	1.16	$y=1.079x–0.591$	0.765	1.62	56
Hsieh *et al.* (2000)	CMOD4	$y=0.903x–0.412$	0.869	0.92	$y=0.925x–0.209$	0.742	1.50	56
	CMOD-IFR2	$y=1.079x–0.951$	0.856	1.14	$y=1.081x–0.597$	0.770	1.59	56
Footprints and proxies								
Hasager *et al.* (2001)	CMOD4	$y=1.043x–1.290$	0.857	1.24	$y=1.070x–1.173$	0.786	1.65	61
	CMOD-IFR2	$y=1.175x–1.539$	0.880	1.23	$y=1.190x–1.307$	0.824	1.58	61

6.3. *Wind direction comparison*

The accuracy of wind direction mapping for SAR wind streaks is of great importance for the reliability of the derived wind-speed maps. Comparison results between *in situ* wind direction data measured at 60 m with a wind vane and averaged from 10-min data to 1-h values centred on the satellite recording time, is graphed in figure 7. A high correlation with $R^2 = 0.97$, a bias of 5° and a standard error of 16° is found. The results are for the 56 cases. Including the five cases of proxy data does not change the statistics.

As explained in §4, the wind direction is determined from 2-D FFT analysis in blocks of 12.5 km × 12.5 km, i.e. there are a total of 64 blocks in each scene with one arrow retrieved per block. However, typically it is not possible to select all arrows due to some blocks being located (partly) over land mass. In table 2 the number of selected arrows is listed per scene. There is one case with only three arrows and several cases with only four to nine arrows. These very low numbers are either due to a small fraction of open sea in the scene, or ill-determined wind direction arrows. Hereafter the number of arrows is expressed as the percentage of selected number of arrows normalized to the number of open ocean arrows.

Relationships are investigated between the derived percentage of SAR streak arrows and the physical conditions on wind speed and static stability. It was possible to select up to 100% arrows in some cases but only 11% in other cases. As expected, more streaks are found in the image spectra for high wind than for low winds (figure 8). The following stability groups are defined: unstable ($Ri < -0.4$ m), neutral ($-0.4\,\text{m} \le Ri \le 0.1$ m), and stable ($Ri > 0.1$). Only near-neutral to slightly unstable conditions allowed more than 40% of the arrows to be selected. For stable conditions less than 25% arrows could be selected. However, also in cases of neutral and unstable conditions does a very low selection number appear (down to 11%). Selecting a low percentage of arrows is only practically feasible due to good information of the *in situ* wind, and a time-consuming selection effort by the user.

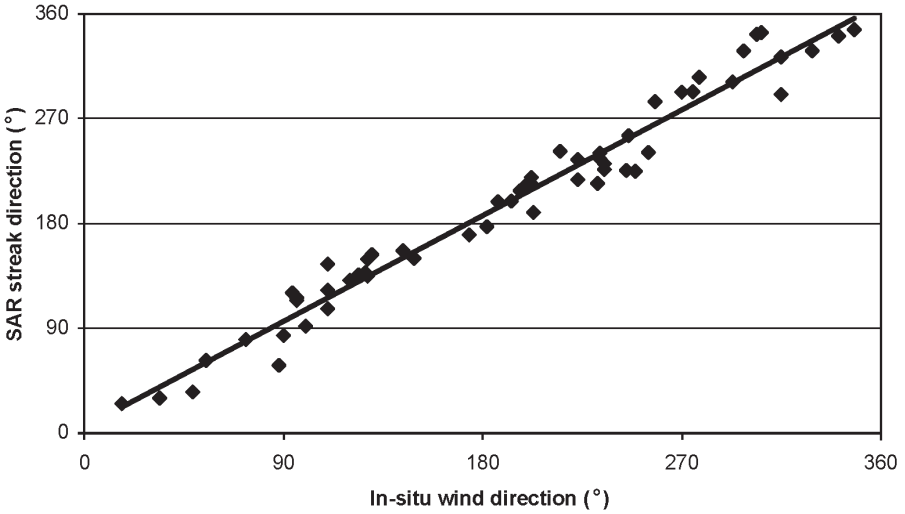

Figure 7. *In situ* wind direction measured at 60 m at the Horns Rev site in the North Sea and SAR wind streak direction found from 2-D FFT and a manual selection of 'good' arrows. A linear regression line is included with $R^2 = 0.968$, bias 5° and SE = 16° for 56 cases.

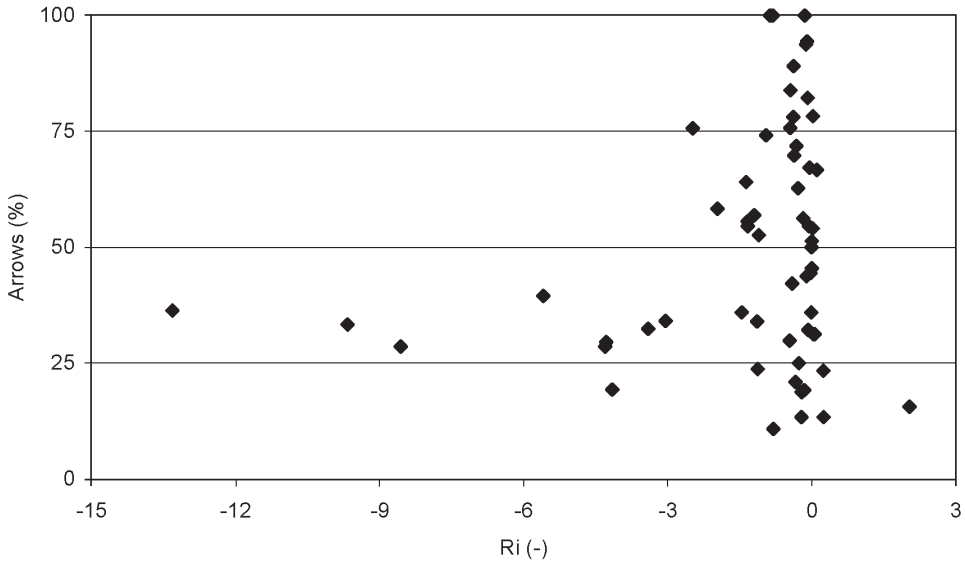

Figure 8. Percentage of selected SAR streak arrows normalized with 'ocean only arrows' found through 2-D FFT in image spectra as a function of the Richardson number (*Ri*). Two outliers, a very unstable situation ($Ri = -146$, 63% arrows) and a very stable ($Ri = 45$, 13% arrows), are omitted from the figure in order to visualize the other data better.

The wind speed in three stability groups is presented as a function of wind direction for all cases in figure 9. Offshore flow is easterly (wind directions between 40° and 140°), onshore flow is westerly (between 220° and 320°) and along-shore flow is either northerly or southerly (the two remaining sectors). Strong wind, i.e. $>10\,\mathrm{m\,s^{-1}}$, mainly occurs under neutral conditions but three unstable offshore flow conditions with high winds are found. Stable conditions are found both for onshore and offshore conditions and typically with low wind speeds. Deviation between *in situ* wind direction and SAR streak direction is analysed in regard to wind speed, wind direction, and atmospheric stability. For wind speeds $>10\,\mathrm{m\,s^{-1}}$, the deviation between *in situ* wind direction and SAR streak direction is always smaller than 20°, whereas for lower wind speeds the error is as high as 38°. The deviation between *in situ* wind direction and SAR streak direction was not found to be a function of wind direction and atmospheric stability.

7. Discussion

Offshore wind-speed maps derived from satellite SAR scenes applying CMOD4 and CMOD-IFR2 scatterometer models to the normalized radar cross-section (Φ_0) are investigated for the Horns Rev site in the North Sea. The relationship between the instantaneous wind field and Φ_0 is well-known, and used here to retrieve spatial snapshots of the wind field in an offshore area for comparison to time-averaged wind observations. The *in situ* wind-speed observations are of very high quality (error $<1\%$), corrected for flow distortion of the meteorological mast, corrected for sea-level changes and averaged in time such as to compare spatial scales to timescales in an appropriate way. Collocation in time and space of the datasets is optimal.

Errors in Φ_0 due to speckle noise, are a major issue, and it is found that for

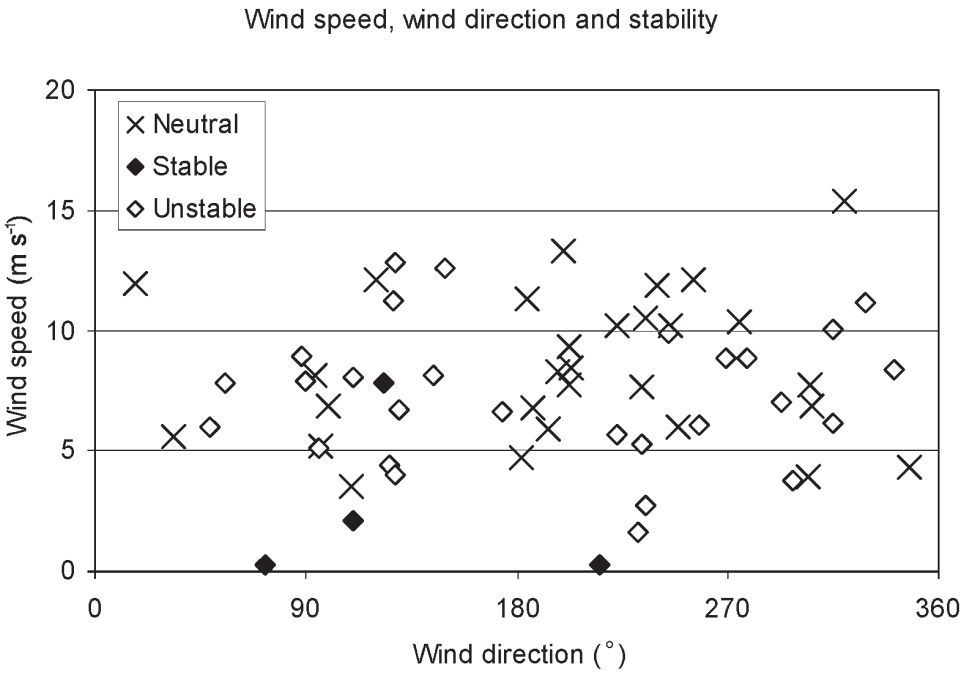

Figure 9. Horns Rev *in situ* observations of atmospheric stability shown as a function of wind direction at 60 m and wind speed at 10 m.

400 m × 400 m grid cells some error is inherent in the wind-speed estimates, around 0.6 m s^{-1} as ENL is ~170 and the noise level is ±0.3 dB. This is below the radiometric accuracy of the instrument (±0.4 dB). Averaging a number of 400 m × 400 m grid cells, e.g. around 25 cells corresponding to ~2000 m × 2000 m grid cells, reduces speckle noise to an insignificant level, <0.2 dB. In fact, the simple footprint method is based on an area-average of this size. According to Stoffelen and Anderson (1997) ±0.2 dB introduces uncertainty on wind ~0.5 m s^{-1}. Multi-looking reduces the speckle noise but also reduces the spatial resolution, hence the trade-off between noise-free data and spatial resolution has to be considered. In an ERS SAR scene from the North Sea acquired under homogeneous wind conditions, Horstmann *et al.* (2000) found that speckle noise is dominating for 100 m × 100 m to 400 m × 400 m pixels. Only for very large grid cells (i.e. 10 km × 10 km) was speckle noise reduced to an insignificant level. Another advantage of a uniform averaging of 25 cells is the reduction of effects of swell.

It is interesting to focus on differences between SAR wind-speed maps derived from an assumption of the SAR wind streaks delineating the wind direction and those where the wind direction is taken from the *in situ* data. Overall the latter gives the best statistics. It is found that R^2 is always higher and standard error (SE) always lower for wind maps calculated from the *in situ* wind direction, but that the bias is always increased, typically ~0.2 to ~0.4 m s^{-1}. A possible explanation may be that an (inherent) bias between SAR streak direction and wind direction, here found to be ~5°, is effectively included in the scatterometer models. (Ekman turning between 60 m and sea level is negligible).

In the current study, the 2-D FFT method of retrieving SAR streak directions is applied including a manual selection procedure. As background information for the

manual selection, knowledge on wind speed from the *in situ* observations is used. It is considered possible to substitute the background wind information with meteorological model results or a nearby land-based met-mast, as it is mainly the 180° ambiguity being removed as well as occasional erroneous vectors aligned parallel to the sides of the 12.5 km × 12.5 km grid cells (figure 2 shows an example).The comparison result between SAR wind streaks and *in situ* wind directions is good. Other methods of retrieving SAR streak directions, such as wavelet analysis (Fichaux and Ranchin 2002, Du *et al*. 2002) or directional wave spectrum modelling (Heron 2002) were not investigated.

Stoffelen and Anderson (1997) find that comparing scatterometer winds at 50 km × 50 km to ECMWF (European Center of Medium Range Forecast) model winds at 200 km × 200 km results in a higher correlation than when comparing scatterometer winds to buoy wind data. The finding indicates that the spatial scale effectively represented by a buoy observation is too small compared to the scatterometer footprint. In other words, scatterometer sub-scale variation is significant (Beal 2000, Monaldo 2000, Thompson *et al*. 2001). Scatterometer models are derived empirically at much larger scales than the SAR. For SAR winds, the spatial scale is around 400 m × 400 m and this scale corresponds very well to the scale represented by *in situ* observations from buoys, ships and masts. Footprint theories describe the likelihood of a meteorological observation to pertain from an area in the upwind direction. The probability density functions (PDF) of three footprint theories are here applied including static stability. From a physical view this is the optimal method. Furthermore, a very simple footprint method assuming neutral conditions and a PDF of equal value over the 90% footprint ellipse is tested. This method allows a suitable number of grid cells to be uniformly averaged reducing speckle noise. The linear regression results show that R^2 and SE are better for the simple footprints than the more advanced footprints. The most likely explanation for this is that speckle noise is more effectively reduced. In the advanced footprint methods one single cell of 400 m × 400 m may be weighted very strongly (up to 75%).

Selecting a box area (proxy) representative of a point in space does not prove very successful in the current study. Box-area SAR wind data are only tested in the few (five) cases where a footprint could not be extracted due to missing data. The linear regression showed a notably higher bias increasing from 0.3 to 1.2 m s^{-1} for $\mathrm{SAR}_{\mathrm{streak\_CMOD4}}$, suggesting that proxy values from box areas should be used with caution.

For the footprints following Gash (1986) the bias is smaller than from the simple footprints (a bias of only −0.1 m s^{-1}, see table 3) but at the same time R^2 is smaller and the standard error is larger. Whether a low bias or a low standard error is most important may depend on the specific application. A graphical display of wind speeds from Hasager *et al*. (2001) and Gash (1986) footprints based on $\mathrm{SAR}_{\mathrm{streak\_CMOD4}}$ and $\mathrm{SAR}_{\mathit{in\ situ}\_\mathrm{CMOD4}}$ wind maps are shown in figure 6(*a*) and (*b*), respectively. It is clear that the regression lines based on wind maps using SAR streak for wind direction are closer to the 1:1 line in both cases. Furthermore, it can be seen that the scatter in the Gash footprint is larger than for the simple footprints especially for higher wind speeds. Correlation results from the stability-corrected footprints of Horst and Weil (1994) and Hsieh *et al*. (2000) show very similar values between them. These, however, are less good than correlation results from the Gash (1986) footprint method. Again, this is most likely due to the heavy weighting of one or few cells and that speckle noise then introduces significant error.

The CMOD4 algorithm provides the best statistical fit to *in situ* wind-speed observations. The linear regression results show a negative bias for both algorithms ranging from $\sim -0.2\,\mathrm{m\,s^{-1}}$ for CMOD4 down to $\sim -1\,\mathrm{m\,s^{-1}}$ for CMOD-IFR2. Systematic variations between the two models are well known and the current dataset is too small for in-depth analysis of, for example, very low and very high wind speeds.

Errors in SAR wind-speed maps caused by atmospheric and oceanic conditions are present in the current dataset. From oceanic conditions, longer-wave tilt modulation is thought to be present on some occasions in the $400\,\mathrm{m} \times 400\,\mathrm{m}$ grid cells, but suppressed effectively at the $4\,\mathrm{km^2}$ scale of the simple footprints. Other oceanic structures possibly related to ocean current, tidal height and bathymetry have been identified. For the tidal flats, unrealistically low values of wind speed have often been observed. Clemente-Colón and Yan (2000) also observed that dark features appear in SAR imagery for extremely shallow regions such as mudflats at low tide. At the North Sea study area, the tidal flats are located more than 30 km from the site of investigation. Synoptic scale atmospheric conditions possibly representing fronts and rain cells were noticed in a few scenes but not near the site of investigation. Rain may reduce σ_0 in C-band SAR by rain volume scattering from atmospheric attenuation and raindrops may impact the sea surface by damping the Bragg waves and thus reduce σ_0 (Clemente-Colón and Yan 2000). No further analysis of these phenomena is considered here. Closer to the site of interest increased and/or reduced wind speeds outlining the shallow reef have been observed in some cases. Such features have been previously described (Romeiser and Alpers 1997, Mastenbroek 1998). Within the current study the use of proxy values instead of footprints for some cases was tested but as the methodology was apt to a subjective selection this was not pursued further.

Very close to the shoreline ($<1\,\mathrm{km}$ offshore) unrealistically low SAR wind speeds are found in all scenes. A slight reduction in wind speed near the coast is anticipated from meteorological models but the reduction observed in the SAR wind maps is much larger. This does not pose a problem in the validation work as the distance from the mast to the shoreline is much longer than a typical footprint. In the few cases where the nonlinear footprints stretch into the near-coast region, a cut-off box is applied. This far upwind ($>13\,\mathrm{km}$) the PDF weight within a footprint is very small. Oceanic noise due to surfactants such as slicks and algal blooms (Espedal *et al.* 1998, Clemente-Colón and Yan 2000) did not seem to appear in the scenes.

The dataset allows a limited investigation on atmospheric conditions and winds from SAR. The major finding is that SAR streaks are most difficult to delineate in low wind conditions. This is in agreement with previous studies (Wackerman *et al.* 1996, Vachon and Dobsen 1996, 2000). It is not possible to conclude whether static stability alone has implications for retrieving SAR wind streaks as four out of five stable cases have low winds, but it seems as near-neutral and weakly unstable conditions allow more SAR streak arrows to be selected in the 2-D FFT procedure than in very unstable conditions.

In summary, the SE is smaller ($\sim 0.9\,\mathrm{m\,s^{-1}}$) for SAR wind maps based on *in situ* wind direction as opposed to SAR streak direction ($\sim 1.3\,\mathrm{m\,s^{-1}}$). This indicates that CMOD scatterometer algorithms are well suited for wind-speed retrieval in SAR, however accurate determination of wind direction remains an important issue in the methodology. The SE can be compared to the uncertainty due to speckle ($0.5\,\mathrm{m\,s^{-1}}$) and calibration ($0.7\,\mathrm{m\,s^{-1}}$) indicating that noise from oceanic and atmospheric

conditions is not the major factor limiting the practical use of SAR wind maps in statistical terms, e.g. for wind resource assessment offshore at the current study site.

A more important limitation for assessing wind resources may be the number of available scenes for a given site. Barthelmie and Pryor (2003) find that 60–70 randomly selected scenes can characterize the mean wind speed and Weibull A parameter but that $\sim$150 scenes and $\sim$2000 scenes are required to give variance and Weibull k, respectively, assuming an uncertainty of $\pm$10% at a confidence level of 90% to be acceptable. SAR scene selections are also restricted in time by satellite overpass times, hence SAR alone is not capable of mapping diurnal wind variations in detail. The advantages of SAR for offshore wind mapping are the high spatial resolution, and the existence of global data in archives.

8. Conclusions

Wind-speed maps derived from ERS-2 SAR scenes using the CMOD4 and CMOD-IFR2 algorithms were compared to offshore *in situ* meteorological observations for 61 cases at the Horns Rev site in the North Sea. It was found that wind speed from CMOD4 is less biased than from CMOD-IFR2, around -0.2 and $-0.6\,\mathrm{m\,s^{-1}}$, respectively, and the SE is smaller for CMOD4. Validation results using a simple footprint averaging technique and three nonlinear footprint methods show the simple footprint method to be more robust with R^2 higher and SE smaller. The better statistical agreement for the simple footprint is explained by the fact that error due to speckle noise is reduced to an insignificant level (ENL $>$ 350; <0.2 dB). From a physical point of view, the *nonlinear* footprints are more accurate than a simple footprint but due to speckle noise at the $400\,\mathrm{m} \times 400\,\mathrm{m}$ grid cell size (ENL $\sim$170; $\sim$0.3 dB) some error is introduced.

SAR streak direction identified by 2-D FFT compares well to *in situ* wind direction with an $R^2 = 0.97$, bias of 5° and SE $= 16^\circ$. There was a statistical improvement using *in situ* wind direction in the CMOD4 and CMOD-IFR2 algorithms rather than the SAR streak direction. The best overall result was $R^2 = 0.88$, bias of $-0.5\,\mathrm{m\,s^{-1}}$ and SE $= 0.9\,\mathrm{m\,s^{-1}}$ for wind-speed maps derived by CMOD4 and averaged by simple footprint compared to *in situ* wind speed. An accurate determination of SAR streak direction remains an important issue to achieve optimal wind maps from imaging SAR, e.g. for the purpose of wind resource assessment based on a series of wind maps.

Acknowledgments

We are grateful to (1) the European Commission for the WEMSAR contract ERK6-CT1999-00017; (2) ESA for the AO3-153 and EO-1356 projects granting the ERS-2 SAR scenes; (3) Elsam Engineering for the meteorological and marine observations at Horns Rev; and (4) the Danish Meteorological Institute and the Royal Danish Administration of Navigation and Hydrography for the tidal observations in Port of Esbjerg. In addition, we thank Dr Henning Skriver, Denmark Technical University for comments on SAR theory and Dr Yaron Levy for comments on the manuscript and language.

Appendix

Hsieh *et al.* (2000) proposed a semi-empirical enhancement of the model of Gash (1986) taking atmospheric stability into account. The footprint length scale is

estimated by

$$A=\frac{Dz_u}{\kappa^2}(z_u/|L|)^{p-1}\text{with}\begin{cases} D=0.28; p=0.59 & z_u/L<-0.04\ \text{(unstable)} \\ D=0.97; p=1 & |z_u/L|\leqslant 0.04\ \text{(neutral)} \\ D=2.44; p=1.33 & z_u/L>0.04\ \text{(stable)} \end{cases} \tag{A1}$$

The new length scale is

$$z_u=z(\ln(z/z_0)-1+z_0/z). \tag{A2}$$

The coefficients (D, p) are calibrated by numerical simulation. Unfortunately the range of height ratio z_0/z in these reference calculations seems too limited for offshore applications, but a power law approximation may be used instead.

Horst and Weil (1994) express the fundamental footprint relation as the upward flux from a surface point source

$$\bar{f}^y(x, z_\mathrm{m})=-\frac{\partial}{\partial x}\int_0^{z_\mathrm{m}} u(z)\frac{c^y(x, z)}{Q}\mathrm{d}z \tag{A3}$$

where Q is the flux, c is the concentration and z_m is the mean plume height. An approximation is provided by insertion of van Ulden's (1978) plume model. The conclusions are that the plume advection relation is mathematically correct in stable conditions and accurate within 10% for unstable conditions. The plume growth-rate relation is accurate within 20%. From the growth rate van Ulden (1978) deduces the distance necessary for the plume to reach a given height as

$$\frac{x}{z_0}=\kappa^{-2}\int_{z_0}^{z_\mathrm{m}}[\ln(sz/z_0)-\psi_\mathrm{m}(sz/L)]\varphi_h(sz/L)\mathrm{d}z\equiv\psi(z_\mathrm{m})-\psi(z_0) \tag{A4}$$

where s is given as $s=r^{1/\mathrm{r}}\Gamma(2/3)/\Gamma(1/r)^{r/(1-\mathrm{r})}$ where $r=1+2m$ and m is found in $u=u_1(z/z_1)^m$. Horst and Weil (1994) calculate the $\Psi(z)$ function from the Businger–Dyer expressions of the non-dimensional profiles.

The crosswind footprint variation is equivalent to the concentration field in a surface plume from a point source according to Horst and Weil (1994). It is usually modelled as a Gaussian distribution with a crosswind spreading growing in the downwind direction. We can express this as

$$f(x, y)=\frac{f^y(x)}{\sqrt{2\pi}\sigma_y(x)}\exp\left\{-\frac{y^2}{2\sigma_y^2(x)}\right\},\quad \text{for } x>0 \tag{A5}$$

Crosswind integration of this two-dimensional footprint formula will reproduce the one-dimensional footprint. Gryning *et al.* (1987) propose a model plume spreading up to distances of 5 km as

$$\sigma_y=\sigma_\mathrm{v}t\Big/\left(1-\sqrt{t/2T_y}\right) \tag{A6}$$

where σ_v is the standard deviation of the crosswind velocity perturbations, $t\approx x/u(z_\mathrm{m})$ is the travel time and T_y is the Lagrangian timescale, which in the lack of accurate information is estimated to 600 s. Gryning *et al.* (1987) recommend the use of measured crosswind velocity perturbations. If unavailable, they could be

modelled by

$$\frac{\sigma_v^2}{u_*^2} = \begin{cases} 0.35(-h/\kappa L)^{2/3} + 2 - z_m/h & \text{for } h/L < 0 \\ 2(1 - z_m/h) & \text{for } h/L > 0 \end{cases} \quad \text{(A7)}$$

where h is the mixing height, which we estimate to 500 m.

References

ASKARI, F., 2001, Multi-sensor remote sensing of eddy-induced upwelling in the southern coastal region of Sicily. *International Journal of Remote Sensing*, **22**, 2899–2910.

ATLAS, R., HOFFMAN, R. N., LEIDNER, S. M., SIENKIEWICZ, J., YU, T.-W., BLOOM, S. C., BRIN, E., ARDIZZONE, J., TERRY, J., BUNGATO, D., and JUSEM, J. C., 2001, The effects of marine winds from scatterometer data on weather analysis and forecasting. *Bulletin of the American Meteorological Society*, **82**, 1965–1990.

ATTEMA, E., DESNOS, Y.-L., and DUCHOSSIOIS, G., 2000, Synthetic aperture radar in Europe: ERS, Envisat, and beyond. *John Hopkins APL Technical Digest*, **21**, 155–169.

BARTHELMIE, R. J., and PRYOR, S. C., 2003, Can satellite sampling of offshore wind speeds realistically represent wind speed distributions? *Journal of Applied Meteorology*, **42**, 83–94.

BASTIAANSSEN, W. G. M., PELGRUM, H., WANG, J., MA, Y., MORENO, J. F., ROERINK, G. J., and VAN DER WAL, T., 1998, A remote sensing surface energy balance algorithm for land (SEBAL)—2. Validation. *Journal of Hydrology*, **213**, 213–229.

BEAL, R. C., 2000, Toward an international storm watch using wide swath SAR. *John Hopkins APL Technical Digest*, **21**, 12–20.

BROWN, R. A., 2000a, On satellite scatterometer model functions. *Journal of Geophysical Research*, **105**, 29 195–29 205.

BROWN, R. A., 2000b, Serendipity in the use of satellite scatterometer, SAR and other sensor data. *John Hopkins APL Technical Digest*, **21**, 21–26.

CLEMENTE-COLÓN, P., and YAN, X.-H., 2000, Low-backscatter ocean features in synthertic aperture radar imagery. *John Hopkins APL Technical Digest*, **21**, 116–121.

DU, Y., VACHON, P. W., and WOLFE, J., 2002, Wind direction estimation from SAR images of the ocean using wavelet analysis. *Canadian Journal of Remote Sensing*, **28**, 498–509.

ESPEDAL, H. A., JOHANNESSEN, O. M., JOHANNESSEN, J. A., DANO, E., LYZENGA, D., and KNULST, J. C., 1998, COASTWATCH'95: a tandem ERS-1/2 SAR detection experiment of natural film on the ocean surface. *Journal of Geophysical Research*, **103**, 24 969–24 982.

FICHAUX, N., and RANCHIN, T., 2002, Combined extraction of high spatial resolution wind speed and direction from SAR images: a new approach using wavelet transform. *Canadian Journal of Remote Sensing*, **28**, 510–516.

FIGA-SALDANÃ, J., WILSON, J. J. W., ATTEMA, E., GELSTHORPE, R., DRINKWATER, M. R., and STOFFELEN, A., 2002, The advanced scatterometer (ASCAT) on the meteorological operational (MetOp) platform: A follow on for European wind scatterometers. *Canadian Journal of Remote Sensing*, **28**, 404–412.

FUREVIK, B. R., and ESPEDAL, H., 2002, Wind energy mapping using synthetic aperture radar. *Canadian Journal of Remote Sensing*, **28**, 196–204.

FUREVIK, B. R., JOHANNESSEN, O., and SANDVIK, A. D., 2002, SAR-retrieved wind in polar regions—comparison with *in situ* data and atmospheric model output. *IEEE Transactions on Geoscience and Remote Sensing*, **40**, 1720–1732.

GARRATT, J. R., 1992, *the Atmospheric Boundary Layer* (New York: Cambridge University Press).

GASH, J. H. C., 1986, A note on estimating the effect of a limited fetch on micrometeorological evaporation measurements. *Boundary-Layer Meteorology*, **35**, 409–413.

GERLING, T. W., 1986, Structure of the surface wind field from the SEASAT SAR. *Journal of Geophysical Research*, **91**, 2308–2320.

GOLDFINGER, A. D., 1982, Estimation of spectra from speckled images. *IEEE Transactions on Aerospace and Electronic Systems*, **AES-18**, NO. 5, 675–681.

GRYNING, S. E., HOLTSLAG, A. A. M., IRWIN, J. S., and SIVERTSEN, B., 1987, Applied dispersion modelling based on meteorological scaling parameters. *Atmospheric Environment*, **21**, 79–89.

HASAGER, C. B., FUREVIK, B., DELLWIK, E., SANDVEN, S., FRANK, H., JENSEN, N. O., ASTRUP, P., JØRGENSEN, B. H., RATHMANN, O., BARTHELMIE, R. J., JOHANNESSEN, O., GAUDIOSI, G., and CHRISTENSEN, L., 2001, Satellite images used in wind resource assessment. *Proceedings of the European Wind Energy Conference (EWEC), 2–6 July 2001*, edited by P. Helm and A. Zervos (Munich: WIP-Renewable Energies), pp. 673–677.

HASAGER, C. B., FRANK, H. P., and FUREVIK, B. R., 2002, On offshore wind energy mapping using satellite SAR. *Canadian Journal of Remote Sensing*, **28**, 80–89.

HERON, M. L., 2002, Applying a unified directional wave spectrum to the remote sensing of wind wave directional spreading. *Canadian Journal of Remote Sensing*, **28**, 346–353.

HORST, T. W., and WEIL, J. C., 1994, How far is far enough—the fetch requirements for micrometeorological measurement of surface fluxes. *Journal of Atmospheric and Oceanic Technology*, **11**, 1018–1025.

HORSTMANN, J., LEHNER, S., KOCH, W., and TONBOE, R., 2000, Computation of wind vectors over the ocean using spaceborne synthetic aperture radar. *John Hopkins APL Technical Digest*, **21**, 100–107.

HSIEH, C. H., KATUL, C., and CHI, T. W., 2000, An approximate analytical model for footprint estimation of scalar fluxes in thermally stratified atmospheric flows. *Advanced Water Research*, **23**, 765–772.

JOHANNESSEN, O. M., and BJÖRGO, E., 2000, Wind energy mapping of coastal zones by synthetic aperture radar (SAR) for siting potential windmill locations. *International Journal of Remote Sensing*, **21**, 1781–1786.

KNAUSS, J. A., 1978, *Introduction to Physical Oceanography* (Englewood Cliffs, New Jersey: Prentice Hall).

KORSBAKKEN, E., JOHANNESSEN, J. A., and JOHANNESSEN, O. M., 1998, Coastal wind field retrievals from ERS synthetic aperture radar images. *Journal of Geophysical Research*, **103**, 7857–7874.

KRAMER, H. J., 1996, *Observation of the Earth and Its Environment*, 3rd edn (Berlin: Springer).

LEHNER, S., HORSTMANN, J., KOCH, W., and ROSENTHAL, W., 1998, Mesoscale wind measurements using recalibrated ERS SAR images. *Journal of Geophysical Research*, **103**, 7847–7856.

LILLESAND, T. M., and KIEFER, R. W., 1987, *Remote Sensing and Image Interpretation*, 2nd edn (New York: John Wiley and Sons).

MASTENBROEK, K., 1998, High-resolution wind fields from ERS SAR. *ESA—Earth Observation Quarterly*, **59**, 20–22.

MONALDO, F., 2000, The Alaska SAR demonstration and near-real-time synthetic aperture radar winds. *John Hopkins APL Technical Digest*, **21**, 75–79.

MONALDO, F. M., THOMPSON, D. R., BEAL, R. C., PICHEL, W. G., and CLEMENTE-COLÓN, P., 2001, Comparison of SAR-derived wind speed with model predictions and ocean buoy measurements. *IEEE Transactions on Geoscience and Remote Sensing*, **39**, 2587–2600.

MOURAD, P. D., 1999, Footprints of atmospheric phenomena in synthetic aperture radar images of the ocean surface: a review. In *Air–Sea Exchange: Physics, Chemistry and Dynamics*, edited by G. L. Geernaert (Dordrecht: Kluwer Academic Publishers), pp. 269–290.

NECKELMANN, S., and PETERSEN, J., 2000, Evaluation of the stand-alone wind and wave measurement systems for Horns Rev 150 kW offshore wind farm in Denmark. *Offshore Wind Energy in Mediterranean and other European Seas (OWEMES) Conference Proceedings, 13–15 April 2000, Sircusa, Sicily, Italy* (Rome: Athena/ENEA), pp. 17–27.

OFFILER, D., 1994, The calibration of ERS-1 satellite scatterometer winds. *Journal of Atmospheric and Oceanic Technology*, **11**, 1002–1017.

OLIVER, C., and QUEGAN, S., 1998, *Understanding Synthetic Aperture Radar Images* (Boston: Massachusetts: Artech House).

QUILFEN, Y., CHAPRON, B., ELFOUHAILY, T., KATSAROS, K., TOURNADRE, J., and

CHAPRON, B., 1998, Observation of tropical cyclones by high-resolution scatterometry. *Journal of Geophysical Research*, **103**, 7767–7786.

ROMEISER, R., and ALPERS, W., 1997, An improved composite surface model for the radar backscattering cross section of the ocean surface. 2. Model response to surface roughness variations and the radar imaging of underwater bottom topography. *Journal of Geophysical Research—Oceans*, **102**, 25 251–25 267.

SIKORA, T. D., THOMPSON, D. R., and BLEIDORN, J. C., 2002, Testing the diagnosis of marine atmospheric boundary-layer structure from synthetic aperture radar. *John Hopkins APL Technical Digest*, **21**, 94–99.

SMEDMAN, A., HOGSTROM, U., BERGSTROM, H., RUTGERSSON, A., KAHMA, K. K., and PETTERSSON, H., 1999, A case study of air–sea interaction during swell conditions. *Journal of Geophysical Research—Oceans*, **104**, 25 833–25 851.

SOMMER, A., 2003, Offshore measurements of wind and waves at Horns Rev and Laesoe, Denmark. *Offshore Wind Energy in Mediterranean and Other European Seas (OWEMES) Conference Proceedings, 10–12 April 2003* (Naples, Italy: Athena), pp. 65–79.

STOFFELEN, A., and ANDERSON, D. L. T., 1993, Wind retrieval and ERS-1 scatterometer radar backscatter measurements. *Advances in Space Research*, **13**, 53–60.

STOFFELEN, A., and ANDERSON, D., 1997, Scatterometer data interpretation: estimation and validation of the transfer function CMOD4. *Journal of Geophysical Research*, **102**, 5767–5780.

STULL, R. B., 1991, *An Introduction to Boundary Layer Meteorology* (Dordrecht: Kluwer Academic).

THOMPSON, D. R., and BEAL, R. C., 2000, Mapping high-resolution wind fields using synthetic aperture radar. *John Hopkins APL Technical Digest*, **21**, 58–67.

THOMPSON, D. R., MONALDO, F. M., BEAL, R. C., WINSTEAD, N. S., PICHEL, W. G., and CLEMENTE-COLÓN, P., 2001, Combined estimates improve high-resolution coastal wind mapping. *EOS, Transactions of the American Geophysical Union*, **82**, 1–3.

VACHON, P. W., and DOBSON, F. W., 1996, Validation of wind vector retrieval from ERS-1 SAR images over the ocean. *Global Atmosphere and Ocean System*, **5**, 177–187.

VACHON, P. W., and DOBSON, E. W., 2000, Wind retrieval from RADARSAT SAR images: selection of a suitable C-band HH polarization wind retrieval model. *Canadian Journal of Remote Sensing*, **26**, 306–313.

VAN ULDEN, A. P., 1978, Simple estimates for vertical diffusion from sources near the ground. *Atmospheric Environment*, **12**, 2125–2129.

WACKERMAN, C., RUFENACH, C. L., SHUCHMAN, R., JOHANNESSEN, J. A., and DAVIDSON, K., 1996, Wind vector retrieval using ERS-1 synthetic aperture radar imagery. *IEEE Transactions on Geoscience and Remote Sensing*, **34**, 1343–1352.